Applied Catalysis B: Environmental 244 (2019) 795–801

Contents lists available at ScienceDirect

Applied Catalysis B: Environmental

journal homepage: www.elsevier.com/locate/apcatb

Synergistic Cu@CoO_x core-cage structure on carbon layers as highly active and durable electrocatalysts for methanol oxidation

Yue Sun[1], Yunjie Zhou[1], Cheng Zhu, Wenjing Tu, Huibo Wang, Hui Huang, Yang Liu*, Mingwang Shao*, Jun Zhong*, Shuit-Tong Lee, Zhenhui Kang*

Institute of Functional Nano & Soft Materials Laboratory (FUNSOM), Jiangsu Key Laboratory for Carbon-Based Functional Materials & Devices, Soochow University, Suzhou, 215123, PR China

ARTICLE INFO

Keywords:
Electrocatalysts
Non-noble metal
Core-cage structure
Methanol oxidation
In-situ X-ray absorption spectroscopy

ABSTRACT

Active and inexpensive electrocatalysts for methanol oxidation reaction (MOR) are highly required for the practical application of direct methanol fuel cells (DMFCs). However, efficient MOR is limited by using the expensive and rare noble metal-based catalysts. Here we report a Cu@CoO_x core-cage nanostructure on carbon layers (CLs) for superior electrocatalysis of MOR in the alkaline media, which shows an excellent specific activity of 150.41 mA cm^{-2} and a high mass activity of 467.94 mA mg^{-1} at the potential of 0.8 V vs. SCE (1.85 V vs. RHE) in 1 M KOH + 1 M CH_3OH. It represents the highest MOR activity ever reported for noble metal-free catalysts. Synchrotron radiation based *in-situ* X-ray absorption spectroscopy reveals that the outside CoO_x cage can form a high Co^{4+} state to easily oxidize methanol, while the adsorption experiments indicate that Cu can act as the methanol adsorption center. The capture-catalysis process on the core-cage structure thus leads to the excellent MOR activity. The CLs can also anchor the Cu@CoO_x particles and accelerate the charge transport to enhance the performance. The Cu@CoO_x-CLs catalyst is economical, abundant, highly active and stable, which has the potential to act as a good alternate material for noble metal-based catalysts in DMFCs.

1. Introduction

Direct methanol fuel cells (DMFCs) are widely considered as a promising power source for portable and mobile applications [1–8]. In DMFCs the key process to determine the efficiency is methanol oxidation reaction (MOR). However, the MOR process typically needs noble metal-based catalysts (such as Pt and Ru) to achieve a high catalytic activity, which are expensive and rare [6–8]. Noble metal-based catalysts also suffer from a short life-time due to catalyst poisoning [6–8]. Alternate catalysts with low cost, abundance, high efficiency and good stability for MOR are thus highly required.

Extensive efforts have been devoted to developing inexpensive and efficient catalysts for MOR. Various non-precious metals, such as Co, Ni, Cu and Mn are widely used due to their excellent catalytic properties and abundance [9–19]. For example, $NiCo_2O_4$, Co_3O_4 and spongy Ni-Mn alloy were reported as efficient catalysts for methanol oxidation [9–11]. Especially, Co-based catalysts involving pure metal, metal oxides, alloys and phosphides were widely investigated for MOR due to their high catalytic activity [10,12–17]. Cu-based catalysts were also used for electrochemical reactions [20]. Interestingly, Cu based materials were reported to show excellent adsorption of methanol molecules [21–23], which could thus be used as the adsorption center for MOR. Actually, Ni and Cu based alloy networks were recently reported to catalyze MOR and showed an excellent specific activity of 84 mA cm^{-2} with a mass activity of 168 mA mg^{-1} [18]. Moreover, the supporting materials of catalysts were also reported to be important for the performance [19,24–27]. For example, by coupling with graphene, CoNi alloy nanoparticles (NPs) showed an excellent specific activity of 110 mA cm^{-2} for MOR [19]. Although the literatures have shown different methods to greatly improve the efficiency of non-precious metal-based catalysts for MOR, unfortunately, by now their catalytic activities are still not high enough [18,19].

Here we report a Cu@CoO_x nanostructure on carbon layers (CLs) for outstanding electrocatalytic methanol oxidation. The Cu@CoO_x-CLs catalyst shows a core-cage structure on CLs, which exhibits a specific activity of 150.41 mA cm^{-2} and a mass activity of 467.94 mA mg^{-1} (after subtracting the baseline current obtained in the absence of methanol) at the potential of 0.8 V vs. SCE (1.85 V vs. RHE). To the best of our knowledge, it represents the highest MOR activity ever reported for noble metal-free catalysts. The Cu@CoO_x-CLs catalyst also shows an

* Corresponding authors.
E-mail addresses: yangl@suda.edu.cn (Y. Liu), mwshao@suda.edu.cn (M. Shao), jzhong@suda.edu.cn (J. Zhong), zhkang@suda.edu.cn (Z. Kang).
[1] These authors contributed equally to this work.

https://doi.org/10.1016/j.apcatb.2018.12.017
Received 11 September 2018; Received in revised form 15 November 2018; Accepted 4 December 2018
Available online 05 December 2018
0926-3373/

excellent long-term durability (≥10,800 s). Synchrotron radiation based *in-situ* X-ray absorption spectroscopy (XAS) is used to probe the reaction mechanism, which reveals that the outside CoO_x cage can form an intermediate Co^{4+} state in MOR to easily oxidize methanol. Adsorption experiments also indicate that Cu can act as the methanol adsorption center. Methanol can thus be captured and catalyzed on the synergistic core-cage structure. The CLs can also enhance the performance by anchoring the particles and accelerating the charge transport [24,26]. The synergistic Cu@CoO_x core-cage nanostructure on CLs act as an affordable, abundant, highly efficient, and stable catalyst for MOR, which thus has great potential to be used in practical applications.

2. Experimental section

2.1. Materials

Cobalt (II) acetate tetra hydrate (CoAc, 99.5%) and copper (II) acetate tetra hydrate (CuAc, 98%) were purchased from Sinopharm chemical Reagent Co., Ltd, and used as received without any further purification. Deionized water was used as solvent, which was obtained from an in-house filtration system (18 MΩ). Carbon dots (CDs) were synthesized via an electrochemical method (see from supporting information) [28].

2.2. Fabrication of yCu@CoO_x-CLs

CoAc and CuAc (totally 300 mg) with different mole ratio were dispersed in 45 mL deionized water (18 MΩ). Then 30 mg CDs (synthesized via an electrochemical method) were added into the solution, followed by ultrasonic treatment for 2 h. The suspension was freeze-dried and calcined at 300 °C for 4 h in nitrogen atmosphere with a heating rate of 3 °C min^{-1}. CDs would form carbon layers under the high temperature by self-assembly. An inductively coupled plasma optical emission spectrometer (ICP-OES, VISTA-MPX (CCD Simultaneous ICP-OES), Varian) was used to measure the metal contents. ICP results of the samples were shown in Table S2. The actual atomic ratio and the nominal atomic ratio are Co : Cu of 1:0.90 for Cu@CoO_x-CLs, 1:2.07 for 2Cu@CoO_x-CLs and 1:3.05 for 3Cu@CoO_x-CLs, respectively.

2.3. Characterization

The phase and crystal structure of the composites were characterized by X-ray powder diffraction (XRD) by using an X'PertProMPD (Holland) D/max-γA X-ray diffractometer with Cu Kα radiation (k = 0.15406 nm) over a 2θ range from 10 to 90°. Raman spectra were recorded on a HR 800 Raman spectroscope (JY, France) equipped with a synapse CCD detector and a confocal Olympus microscope. The spectrograph used 600 g mm^{-1} gratings and a 633 nm He-Ne laser. Transmission electron microscopy (TEM) and high-resolution TEM (HRTEM) images were observed by an FEI TecnaiF20 transmission electron microscope operating at 200 kV. The Fourier transform infrared (FT-IR) spectrum was collected by using a Nicolet 360 spectrometer. X-ray photoelectron spectroscopy (XPS) was performed by KRATOS Axis ultra DLD X-ray photoelectron spectrometer with monochromatised Mg Kα X-rays (hν = 1253.6 eV). The *in-situ* X-ray absorption spectroscopy (XAS) data were collected on beamline 1W1B at the Beijing Synchrotron Radiation Facility (BSRF) using an *in-situ* reaction cell.

2.4. Electrochemical measurements

Electrochemical measurements were conducted using a CHI660E electrochemical analysis instrument. A saturated calomel electrode (SCE), carbon rod and glassy carbon with diameter of 3 mm were used as the reference, counter and working electrodes, respectively. 3 mg of the synthesized yCu@CoO_x-CDs was added in 400 μL of 0.5 wt% Nafion solution and sonicated for 30 min to ensure a good dispersion. Then 3 μL of the ink was dipped on the working electrode surface and dried at room temperature for the measurements. The loading capacity of the catalysts is 0.32 mg cm^{-2}, which keeps a consistent value for all the samples for suitable comparison. A solution of 1 M KOH and a mixture of 1 M KOH and 1 M CH_3OH are used as the electrolytes for CV and MOR, respectively. The MOR current densities are measured with respect to the geometric area of the glassy carbon electrode (GCE). Electrochemical impedance spectroscopy (EIS) was performed using a GCE at frequencies between 100 kHz and 100 Hz.

3. Results and discussion

3.1. Characterization of electrocatalysts

The synthesis process of yCu@CoO_x-CLs is provided in the Supporting Information. Field-emission scanning electron microscopy (FESEM) images of the yCu@CoO_x-CLs catalysts with various Co : Cu ratios are shown in Fig. S1. It is clear that particles with different size are deposited on CLs. CLs come from the self-assembly of carbon dots (CDs) precursors under high temperature. CDs were synthesized via an electrochemical method reported in the literature [28]. The microstructure of 2Cu@CoO_x-CLs is further studied by TEM shown in Fig. 1. Fig. 1a reveals that the particles on CLs have a uniform size around 60 nm. The insert shows the TEM image of a single particle, revealing an inner core with a 40 nm diameter (white dash line) and an outside layer around 10 nm thick (red dash line). The high-resolution TEM (HRTEM) image of the particle is shown in Fig. 1b, exhibiting a solid core and a porous cage. The porous structure has been marked by red dashed ovals. Further HRTEM images in Fig. 1c and 1d show the crystal structure of the core and the cage labeled by white and blue squares in Fig. 1b, respectively. Fig. 1c clearly identifies the (111) crystalline phase of Cu metal with a lattice spacing of 0.21 nm, while Fig. 1d shows the (311) crystalline phase of Co_3O_4 with a lattice spacing of 0.24 nm. The results suggest a Cu metal core with a Co_3O_4 cage structure in 2Cu@CoO_x-CLs. The core-cage structure can be further confirmed by the elemental mappings using high-angle annular dark-field scanning transmission electron microscopy (HAADF-STEM) shown in Fig. 1e–j. The Cu core can be clearly observed in Fig. 1i and the Co based hollow cage structure (porous shell) can be identified in Fig. 1h. Fig. 1j also shows the overlapped Cu and Co mapping, confirming the core-cage structure.

Fig. S2 shows the XRD patterns of 2Cu@CoO_x-CLs. The main peaks at 43.3°, 50.4°, and 74.1° can be index to the (111), (200), and (220) planes of Cu metal (JCPDS 04-0836), strongly indicating the existence of Cu metal core. The peak at 36.9° can be assigned to the (111) plane of Co_3O_4 (JCPDS 42-1467). The weak intensity can be attributed to the thin porous structure of Co_3O_4 in the sample. The XRD spectra of Cu@CoO_x-CLs and 3Cu@CoO_x-CLs are also shown in Fig. S2 with similar crystal structure. The FT-IR and Raman spectra of 2Cu@CoO_x-CLs are shown in Fig. S3. Abundant oxygen-containing groups such as C═O and O—H can be observed from the FT-IR spectrum. The Raman spectrum confirms the graphite structure of the CLs with an intensity ratio of D and G bands (I_D/I_G) around 1.29, which is slightly higher than that of CDs (I_D/I_G = 1.11, Fig. S4).

X-ray photoelectron spectroscopy (XPS) is used to investigate the electronic structure of 2Cu@CoO_x-CLs. At Co 2p edge (Fig. S5a), the XPS spectrum of 2Cu@CoO_x-CLs can be deconvoluted into three components, corresponding to Co^0, Co^{2+} and Co^{3+} along with two shake-up satellites. The main components in 2Cu@CoO_x-CLs are Co^{2+} and Co^{3+} with strong features, indicating the presence of Co_3O_4 in good agreement with the TEM and XRD results [26,29]. The weak Co^0 signal may come from the interface between Co and Cu. The Cu 2p XPS spectrum is shown in Fig. S5b, exhibiting a main peak for Cu^0/Cu^+

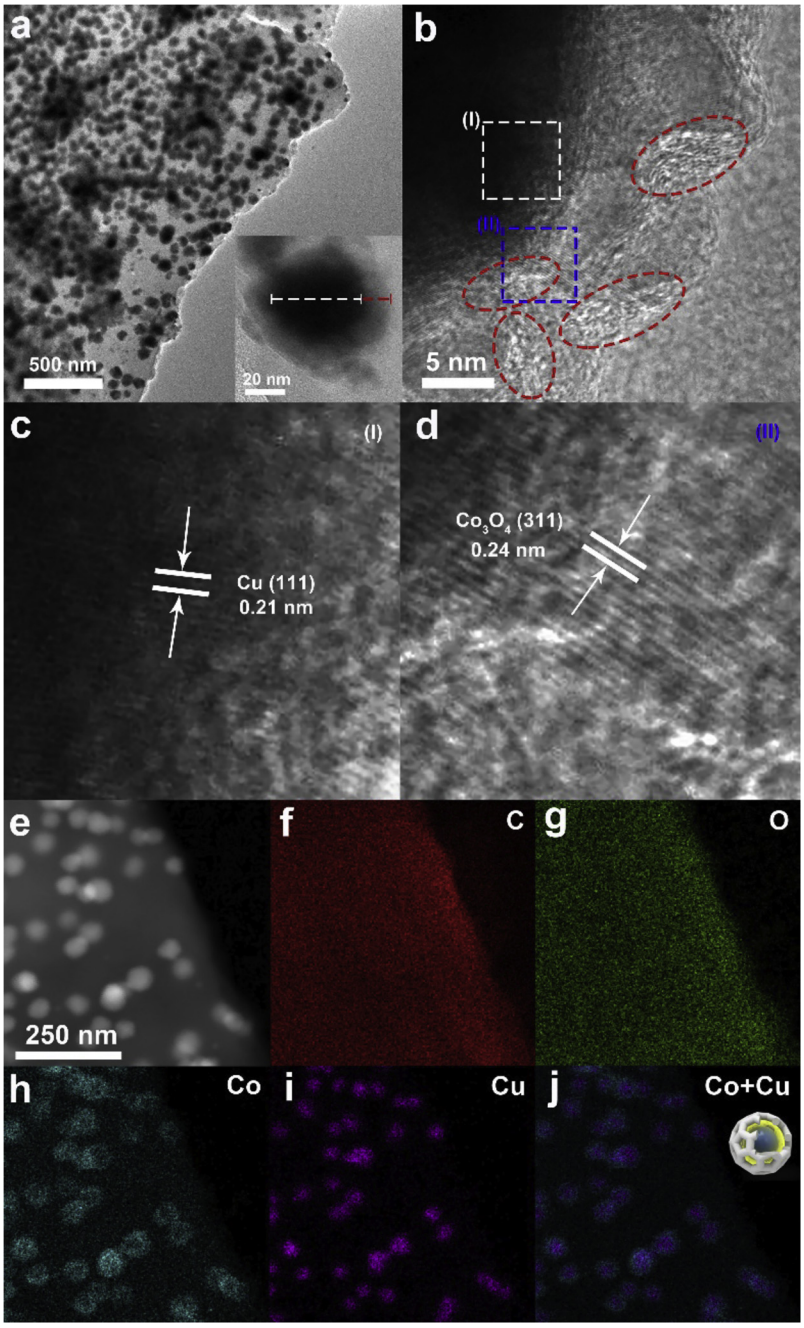

Fig. 1. Morphology and structure characterization of 2Cu@CoO_x-CLs composite. (a) TEM image of 2Cu@CoO_x-CLs catalyst (the insert shows a single 2Cu@CoO_x-CLs particle). (b) HRTEM image of 2Cu@CoO_x-CLs. (c) and (d): the magnified views in (b) (white square for (c) and blue square for (d)). (e–j): HAADF-STEM image of 2Cu@CoO_x-CLs core-cage particles (e) and the corresponding elemental mappings: C (f), O (g), Co (h), Cu (i), Co + Cu (j). (For interpretation of the references to colour in this figure legend, the reader is referred to the web version of this article).

signal with a weak Cu^{2+} peak [30]. The oxidized Cu states may come from the exposed parts of the Cu core through the porous cage structure, while the core is mainly Cu^0 according to the TEM and XRD results. The C 1s XPS spectrum is also shown in Fig. S5c, which can be deconvoluted into three peaks for C═C, C—O and C═O bonds [25]. Fig. S5d also shows the O 1s spectrum with various oxidized peaks.

3.2. Electrocatalytic properties

The electrocatalytic activity of yCu@CoO_x-CLs is measured in 1 M KOH at a scan rate of 50 mV s^{-1}. To convert the SCE scale into RHE scale, the linear sweep voltammetry (LSV) curves of hydrogen evolution versus SCE at a Pt wire in the 1 M KOH and 1 M KOH + 1 M CH_3OH were calculated and shown in Fig. S6. The results show that the onset potential of hydrogen evolution versus SCE at a Pt wire in 1 M KOH and 1 M KOH + 1 M CH_3OH are all about 1.05 V vs. SCE. Fig. 2a compares the CV curves of yCu@CoO_x-CLs with different Co : Cu ratios (n(Co) : n (Cu) = 1 : 1, 1 : 2 and 1 : 3). In the forward scan, the wide peak at about +0.18 V vs. SCE can be assigned to the Co^{2+}/Co^{3+} redox process, while that at about +0.53 V vs. SCE can be attributed to the Co^{3+}/Co^{4+} redox process. In the backward scan, the wide peaks at about +0.25 V and +0.02 V (vs. SCE) can be assigned to the reduction processes of Co^{4+} and Co^{3+}, respectively [31–34]. Obviously, the oxidation peak current density for 2Cu@CoO_x-CLs is higher than that for Cu@CoO_x-CLs and 3Cu@CoO_x-CLs, suggesting more active sites. Fig. S7 shows the surface coverage results of Co^{3+}/Co^{4+} redox species (Γ^*) in

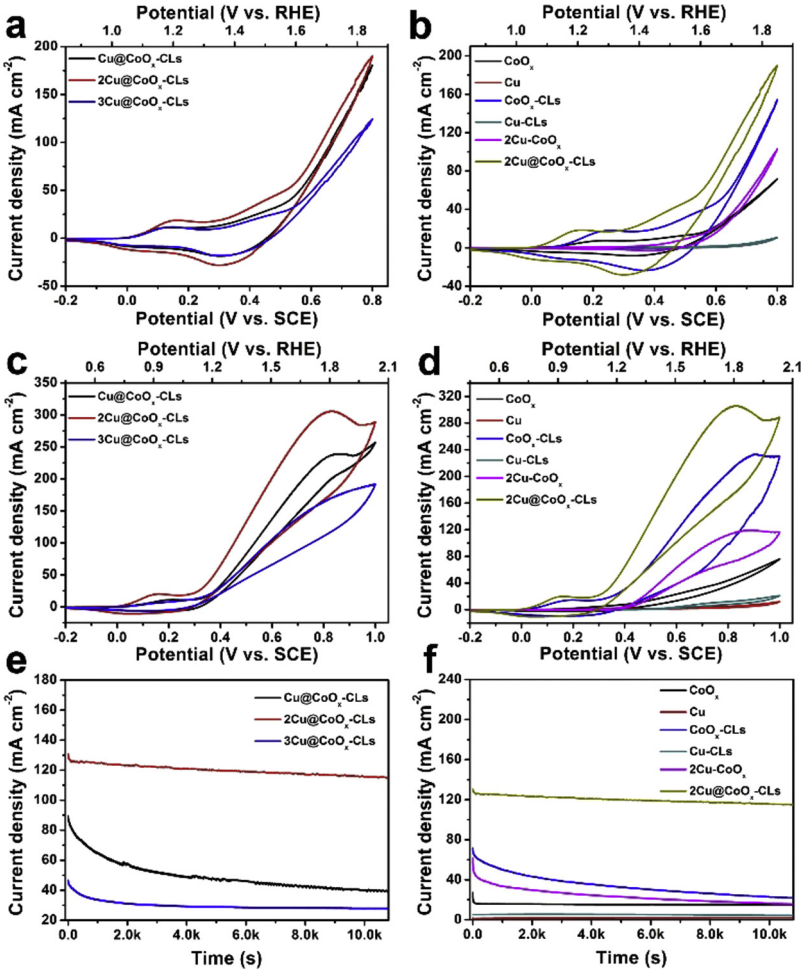

Fig. 2. Electrochemical characterization. (a) CV curves of yCu@CoO_x-CLs samples with different Co: Cu ratios in 1 M KOH. (b) CV curves of 2Cu@CoO_x-CLs and the reference samples in 1 M KOH. (c) CV curves of yCu@CoO_x-CLs samples in 1 M KOH + 1 M CH_3OH. (d) CV curves of 2Cu@CoO_x-CLs and the reference samples in 1 M KOH + 1 M CH_3OH. (e) Chronoamperograms of yCu@CoO_x-CLs in 1 M KOH + 1 M CH_3OH at 0.5 V vs. SCE (1.55 V vs. RHE). (f) Chronoamperograms of 2Cu@CoO_x-CLs and the reference samples in 1 M CH_3OH +1 M KOH at 0.5 V vs. SCE (1.55 V vs. RHE). All the curves are collected at a scan rate of 50 mV s^{-1}.

the yCu@CoO_x-CLs electrodes. The Γ^* value for 2Cu@CoO_x-CLs is calculated to be 8.83×10^{-6} mol cm^{-2}, which is slightly higher than that for Cu@CoO_x-CLs (7.07×10^{-6} mol cm^{-2}) and 3Cu@CoO_x-CLs (7.01×10^{-6} mol cm^{-2}). The higher oxidation peak current density for 2Cu@CoO_x-CLs can be partly attributed to the larger surface coverage of redox species [18].

Fig. 2c shows the electrochemical behaviors of yCu@CoO_x-CLs for MOR in 1 M KOH + 1 M CH_3OH. It is clear that the 2Cu@CoO_x-CLs sample shows the best performance with a highest peak current density of 305.4 mA cm^{-2} at + 0.83 V vs. SCE (1.88 V vs. RHE), which is 1.3 times of that of Cu@CoO_x-CLs (238.4 mA cm^{-2}) and 1.7 times of that of 3Cu@CoO_x-CLs (176.9 mA cm^{-2}). In addition, the current density at 0.83 V vs. SCE (1.88 V vs. RHE) can also be partly attributed to the oxygen evolution process. 2Cu@CoO_x-CLs also shows a more negative onset potential (~ 0.26 V) than that of Cu@CoO_x-CLs (~ 0.30 V) and 3Cu@CoO_x-CLs (~ 0.31 V) (vs. SCE). When subtracting the corresponding baseline current obtained in absence of methanol (also see Fig. S8), the peak current density of 2Cu@CoO_x-CLs shows a high specific activity of 150.41 mA cm^{-2}, which represents the best catalytic value for MOR ever reported for noble metal-free catalysts (Table S1). Moreover, when calculating the mass activity according to the ICP data (Table S2), it is also as high as 467.94 mA mg^{-1} (value calculated based on all metal and CLs). The results suggest that the present 2Cu@CoO_x-CLs sample is a superior noble metal-free catalyst for MOR with an outstanding electrocatalytic performance. It should also be noted that the working potential at 0.83 V vs. SCE is higher than that used for noble metal-based catalysts and this needs improvement for future application.

The 2Cu@CoO_x-CLs catalyst with outstanding MOR activity also shows excellent stability demonstrated by chronoamperometry. Fig. 2e shows the chronoamperograms of yCu@CoO_x-CLs at a potential step of 0.5 V vs. SCE (1.55 V vs. RHE) in 1 M KOH + 1 M CH_3OH for 10,800 s. All the three catalysts show a sharp initial decay and a following slight decrease. The initial high activity can be attributed to the fast kinetic reaction and then the sharp decrease due to the slow kinetic reaction with the active sites occupied by the adsorbed intermediates [18]. For the following slight decrease, it might be assigned to the poisoning of active catalytic sites [18]. The activities of Cu@CoO_x-CLs and 3Cu@CoO_x-CLs show a sharp decay (50% left), while 2Cu@CoO_x-CLs exhibits a current density of 115.16 mA cm^{-2} with 88% of its initial activity left. The presented chronoamperometric stability of 2Cu@CoO_x-CLs is also better than the Pt and Pd-besed catalysts for MOR reported in the literatures [7,35–38]. To further confirm the stability of 2Cu@CoO_x-CLs, the stability experiments for 100 h was carried out and the results are shown in Fig. S9. Since methanol oxidation in KOH can also produce CO_2 and lead to the formation of carbonates, which will reduce the conductivity and adsorb on the electrode to lower the performance. It can be observed that after 100 h, the current density decreases to 77.47 mA cm^{-2}, which is 59% of its initial activity. Fig. S10 also shows the Nyquist plots of electrochemical impedance spectroscopy (EIS) to

probe the reaction kinetics of yCu@CoO_x-CLs, in which 2Cu@CoO_x-CLs shows the smallest diameter of the semicircle suggesting the lowest charge transfer resistance [14]. The electrochemical active area (ECSA) of yCu@CoO_x-CLs is also probed, while the samples with various Co : Cu ratios show almost no difference (Fig. S11).

The electrocatalytic activities of various reference samples such as CoO_x, Cu, CoO_x-CLs, Cu-CLs, and 2Cu-CoO_x are also compared with that of 2Cu@CoO_x-CLs in Fig. 2. Fig. 2f also shows the long-term activity and stability until 10,800 s. Interestingly, the MOR activities of Cu-based catalysts (Cu and Cu-CLs) are very low, while all Co-based catalysts show much better activities (Fig. 2d). The results suggest that Co is the main catalytic element for MOR. Both Cu and CLs can significantly enhance the performance of Co-based catalysts. Especially, the combination of Cu, Co and CLs with suitable elemental ratios in 2Cu@CoO_x-CLs shows the best performance. It is well known that carbon materials can serve as good supporting materials to anchor the particles and facilitate charge transfer, which can thus greatly improve the catalytic performance [26,27]. Cu also plays a key role in MOR reaction. It was widely reported that Cu (Cu^{2+}) showed an excellent capability to adsorb methanol molecules with hybridized electronic structure [21–23]. Thus the Cu core in 2Cu@CoO_x-CLs can act as an adsorption center to capture the surrounding methanol molecules.

3.3. Research on electrocatalytic mechanism

To verify the excellent methanol adsorption capability of Cu, methanol adsorption curves for various samples are shown in Fig. 3. 10 mg of 2Cu@CoO_x-CLs catalysts was added into a 5 mL reactor while another empty reactor was used for comparison. Subsequently, 10 μL of saturated methanol steam was injected into the two 5 mL reactors. After standing still for predetermined time intervals, the residual concentration of methanol in the reactor was determined by an Agilent gas chromatography (details can be obtained from Section 1.3 in Supporting information). The residual concentration percentages of CoO_x-CLs, CLs, 2Cu@CoO_x-CLs and Cu-CLs after 80 min are 76.17%, 73.32%, 56.14% and 24.50%, respectively. Accordingly, the amounts of adsorbed methanol are about 0.05 mg g^{-1}, 0.06 mg g^{-1}, 0.1 mg g^{-1} and 0.16 mg g^{-1}. These data reveal that Cu-based materials have much better methanol adsorption capability than those of Co-based materials or pure CLs, strongly confirming the excellent methanol adsorption of the Cu core. With the assistance of Cu core, the CoO_x cage at a high chemical state can thus act as an efficient catalytic center for MOR [12–17]. Also, the core-cage structure can strongly enhance the reaction interface to accelerate the catalytic process.

Fig. 4a also shows the correlation between the methanol concentration and the electrocatalytic performance. With the existence of CH_3OH, 2Cu@CoO_x-CLs exhibits a typical electrochemical response. Moreover, the oxidation peaks show a positive shift with the increased methanol concentration, indicating a higher oxidation potential with more adsorbed methanol. The oxidation peak current density is also proportional to the methanol concentration in Fig. 4b, suggesting that the reaction is a diffusion-control process. The amount of CDs is also optimized and the results are shown in Fig. S12.

The MOR catalytic process is probed by synchrotron radiation based *in-situ* XAS experiments at both Co and Cu *K*-edges. The XAS data are shown in Fig. 5. Fig. 5a shows the Co *K*-edge XAS spectra of 2Cu@CoO_x-CLs at the applied potential of 0 V, 0.18 V, 0.83 V and back to 0 V (vs. SCE), respectively. The spectrum at 0 V stands for the 2Cu@CoO_x-CLs electrode immersed in 1 M KOH + 1 M CH_3OH without external bias, while the spectra at 0.18 V and 0.83 V stand for the samples in the MOR reaction. Especially, the spectrum at 0.83 V reveals the chemical state of Co to produce the peak current density in the MOR process. The spectrum back to 0 V stands for the sample after the reaction and without external bias.

The spectrum at 0 V vs. SCE shows a peak position and a spectral shape similar to that of standard Co_3O_4, which can be further confirmed in Figs. S13a and S13b [27]. The result is consistent with the above discussion. However, an obvious positive energy shift can be observed when an external potential of 0.18 V vs. SCE is applied, suggesting a higher chemical state of Co at 0.18 V vs. SCE. It can be attributed to the Co^{2+}/Co^{3+} redox process, which is confirmed by the XAS data in Fig. S13 with a Co_2O_3 state. Moreover, when the external potential is 0.83 V vs. SCE, the XAS spectrum shows a further positive energy shift, strongly identifying the presence of a higher Co^{4+} intermediate state. The shift is small but clear, which can be clearly observed in the inset of Figs. 5a and S14 with more applied voltage steps. The highly oxidized Co^{4+} state can thus easily oxidize methanol and then accelerate the MOR process [39], which will finally improve the catalytic efficiency. When the reaction is finished (back to 0 V vs. SCE), the spectrum can recover to the initial state (similar energy position), confirming the reversible Co as a good catalyst. The *in-situ* XAS experiments at Co *K*-edge clearly reveal that Co is the main catalytic element with highly tunable chemical states at different potentials.

The Cu *K*-edge XAS spectra of 2Cu@CoO_x-CLs at the applied potential of 0 V, 0.18 V, 0.83 V and back to 0 V (vs. SCE) are also shown in Fig. 5b. The spectrum at 0 V vs. SCE suggests that Cu in the catalyst is mainly Cu metal with a partly oxidized CuO shell, which can be clearly observed in Figs. S15a and S15b with a comparison to the reference samples [27]. When an external bias of 0.18 V vs. SCE is applied, the Cu spectrum shows a slight increase of the peak intensity, indicating a slight oxidization (Extended X-ray Absorption Fine Structure (EXAFS) data also see Fig. S15b). However, the Cu core is mainly Cu metal with a slightly oxidized shell. The spectrum at a higher potential of 0.83 V vs. SCE shows almost no change when compared to that at 0.18 V vs. SCE, suggesting Cu is not sensitive to the MOR process and is not the main catalytic element. The spectrum back to 0 V vs. SCE is also very similar to that at 0.18 V, suggesting Cu is not a reversible catalyst.

The *in-situ* XAS experiments reveal that Co is the main catalytic element for efficient MOR while the methanol adsorption experiments indicate that Cu can play a key role as the methanol adsorption center.

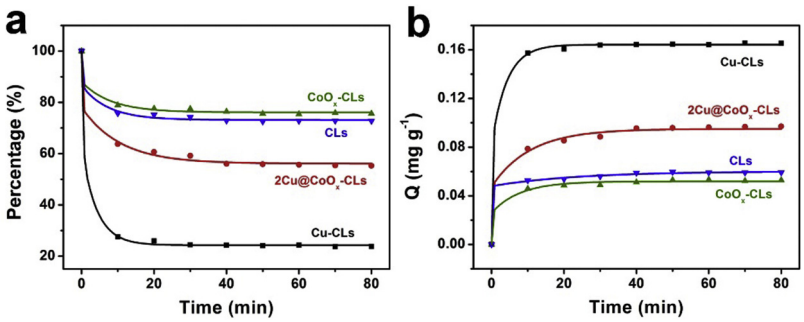

Fig. 3. The time-course adsorption of methanol by CoO_x-CLs, CLs, 2Cu@CoO_x-CLs and Cu-CLs catalysts. (a) The relationship between the residual content of methanol in the system and the adsorption time. (b) The relationship between the amount of adsorbed methanol and the adsorption time.

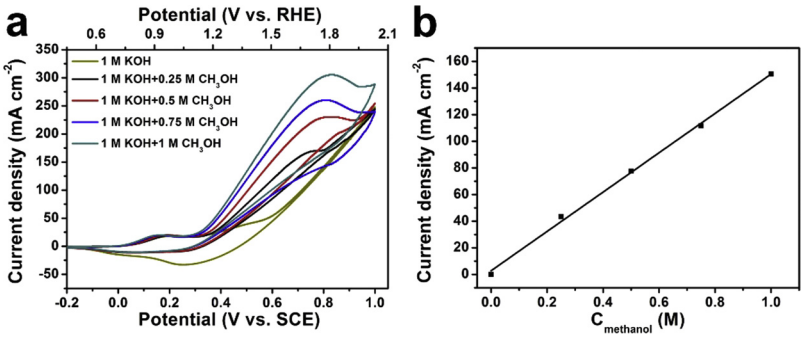

Fig. 4. The correlation between the methanol concentration and the electrocatalytic performance. (a) CV curves of 2Cu@CoO_x-CLs in 1 M KOH solution in the presence of different concentrations of methanol (0, 0.25, 0.5, 0.75 and 1 M) at a scan rate of 50 mV s^{-1}. (b) Relationship between the oxidation peak current density (the baseline current obtained in KOH has been subtracted) and the methanol concentration.

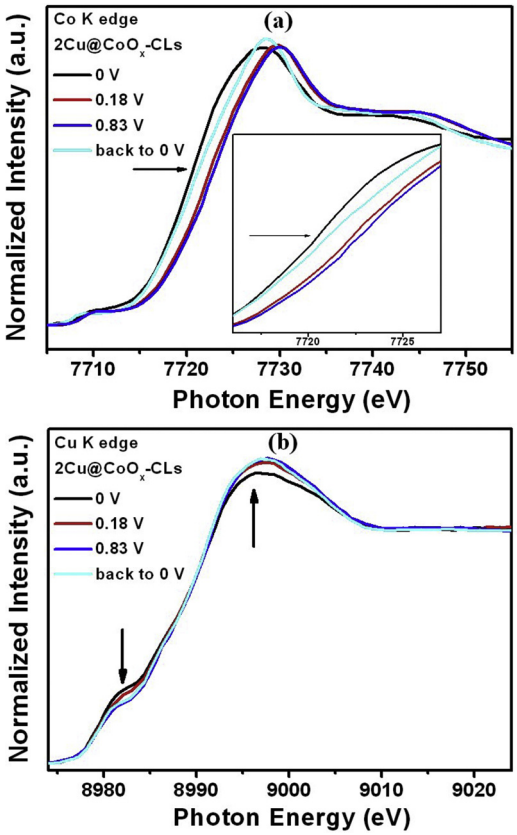

Fig. 5. Synchrotron radiation based *in-situ* XAS experiments at both Co and Cu *K*-edges. (a) Co *K*-edge XAS spectra of 2Cu@CoO_x-CLs at the potential of 0 V, 0.18 V, 0.83 V and back to 0 V (vs. SCE), respectively; (b) Cu *K*-edge XAS spectra of 2Cu@CoO_x-CLs at the potential of 0 V, 0.18 V, 0.83 V and back to 0 V (vs. SCE), respectively.

The carbon layers can also anchor the particle with good charge transport properties. Thus the 2Cu@CoO_x-CLs catalyst with a core-cage-support structure can show a synergetic effect of Cu, CoO_x and CLs to achieve the excellent MOR activity. The catalytic mechanism is also illustrated in Fig. 6. The Cu core (Cu^0/Cu^{2+}) serves as an adsorption center to capture the surrounding methanol molecules (labeled as the first step), and then the CoO_x cage can effectively catalyze the adsorbed methanol molecules with a high chemical state of Co^{4+} (the second step). The carbon layers help to anchor the particles and facilitate charge transport between the CoO_x cage and the electrode. An excellent MOR efficiency can thus be obtained.

4. Conclusion

In this work, we report a Cu@CoO_x core-cage nanostructure deposited on CLs for the superior electrocatalysis of MOR. The catalyst shows an excellent specific activity of 150.41 mA cm^{-2} and an outstanding mass activity of 467.94 mA mg^{-1} at the potential of 0.8 V vs. SCE (1.85 V vs. RHE), which is the highest methanol oxidation activity ever reported for noble metal-free catalysts. It also shows an impressive long-term durability (≥ 10,800 s). Adsorption experiments indicate that Cu can act as the methanol adsorption center. Then the CoO_x cage with an intermediate Co^{4+} state in MOR can effectively catalyze the reaction, which is clearly revealed by the *in-situ* XAS experiments. The carbon layers help to anchor the particles and accelerate the charge transport between the CoO_x cage and the electrode. The synergistic Cu@CoO_x core-cage nanostructure on CLs can thus act as an affordable, abundant, highly efficient, and stable catalyst for MOR, which might serve in the practical applications in the future.

Acknowledgements

This work is supported by the Collaborative Innovation Center of Suzhou Nano Science and Technology, the National Natural Science Foundation of China (51725204, 51572179, 21471106, 21771132, 21501126, U1732110), the Natural Science Foundation of Jiangsu Province (BK20161216), the 111 Project and a project funded by the

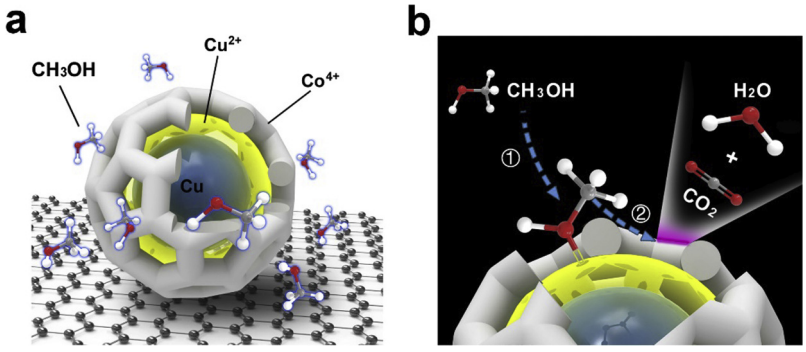

Fig. 6. Schematic illustration of methanol oxidation on 2Cu@CoO_x-CLs.

Priority Academic Program Development of Jiangsu Higher Education Institutions (PAPD). We also thank BSRF for the support of XAS experiments.

Appendix A. Supplementary data

Supplementary material related to this article can be found, in the online version, at doi:https://doi.org/10.1016/j.apcatb.2018.12.017.

References

[1] P. Simon, Y. Gogotsi, Materials for electrochemical capacitors, Nanosci. Technol. 7 (2008) 845–854, https://doi.org/10.1142/9789814287005_0033.

[2] C. Bianchini, P.K. Shen, Palladium-based electrocatalysts for alcohol oxidation in half cells and in direct alcohol fuel cells, Chem. Rev. 109 (2009) 4183–4206, https://doi.org/10.1021/cr9000995.

[3] A.S. Aricò, P. Bruce, B. Scrosati, J.M. Tarascon, W.V. Schalkwijk, Nanostructured materials for advanced energy conversion and storage devices, Nat. Mater. 4 (2005) 366–377, https://doi.org/10.1142/9789814317665_0022.

[4] R. Bashyam, P. Zelenay, A class of non-precious metal composite catalysts for fuel cells, Nature 443 (2006) 63–66, https://doi.org/10.1142/9789814317665_0034.

[5] M. Winter, R.J. Brodd, What are batteries, fuel cells, and supercapacitors? Chem. Rev. 104 (2004) 4245–4270, https://doi.org/10.1021/cr020730k.

[6] J. Chang, L. Feng, C. Liu, W. Xing, X. Hu, Ni_2P enhances the activity and durability of the Pt anode catalyst in direct methanol fuel cells, Energy Environ. Sci. 7 (2014) 1628–1632, https://doi.org/10.1039/c4ee00100a.

[7] W. Huang, H. Wang, J. Zhou, J. Wang, P.N. Duchesne, D. Muir, P. Zhang, N. Han, F. Zhao, M. Zeng, J. Zhong, C. Jin, Y. Li, S.T. Lee, H. Dai, Highly active and durable methanol oxidation electrocatalyst based on the synergy of platinum-nickel hydroxide-graphene, Nat. Commun. 6 (2015) 10035–10043, https://doi.org/10.1038/ncomms10035.

[8] M.E. Scofield, C. Koenigsmann, L. Wang, H. Liu, S.S. Wong, Tailoring the composition of ultrathin, ternary alloy PtRuFe nanowires for the methanol oxidation reaction and formic acid oxidation reaction, Energy Environ. Sci. 8 (2015) 350–363, https://doi.org/10.1039/C4EE02162B.

[9] T.H. Ko, K. Devarayan, M.K. Seo, H.Y. Kim, B.S. Kim, Facile synthesis of core/shell-like $NiCo_2O_4$-decorated MWCNTs and its excellent electrocatalytic activity for methanol oxidation, Sci. Rep. 6 (2016) 20313–20322, https://doi.org/10.1038/srep20313.

[10] J.B. Wu, Z.G. Li, X.H. Huang, Y. Lin, Porous Co_3O_4/NiO core/shell nanowire array with enhanced catalytic activity for methanol electro-oxidation, J. Power Sources 224 (2013) 1–5, https://doi.org/10.1016/j.jpowsour.2012.09.085.

[11] O. Aaboubi, A.Y. Ali-Omar, E. Dzoyem, J. Marthe, M. Boudifa, Ni-Mn based alloys as versatile catalyst for different electrochemical reactions, J. Power Sources 269 (2014) 597–607, https://doi.org/10.1016/j.jpowsour.2014.06.145.

[12] Z.K. Ghouri, N.A.M. Barakat, M. Obaid, J.H. Lee, H.Y. Kim, Co/CeO_2-decorated carbon nanofibers as effective non-precious electro-catalyst for fuel cells application in alkaline medium, Ceram. Int. 41 (2015) 2271–2278, https://doi.org/10.1016/j.ceramint.2014.10.031.

[13] W. Su, Y. Fu, T. Wang, Y. Yu, J. Hu, A cobalt nanoparticle ion-implantation-modified indium tin oxide electrode for direct electrocatalytic oxidation of methanol in alkaline media, RSC Adv. 5 (2015) 79178–79183, https://doi.org/10.1039/C5RA14313F.

[14] L. Qian, L. Gu, L. Yang, H. Yuan, D. Xiao, Direct growth of $NiCo_2O_4$ nanostructures on conductive substrates with enhanced electrocatalytic activity and stability for methanol oxidation, Nanoscale 5 (2013) 7388–7396, https://doi.org/10.1039/c3nr01104f.

[15] M.U.A. Prathap, R. Srivastava, Synthesis of $NiCo2O_4$ and its application in the electrocatalytic oxidation of methanol, Nano Energy 2 (2013) 1046–1053, https://doi.org/10.1016/j.nanoen.2013.04.003.

[16] X. Cui, W. Guo, M. Zhou, Y. Yang, Y. Li, P. Xiao, Y. Zhang, X. Zhang, Promoting effect of Co in Ni_mCo_n ($m + n = 4$) bimetallic electrocatalysts for methanol oxidation reaction, ACS Appl. Mater. Inter. 7 (2015) 493–503, https://doi.org/10.1021/am506554b.

[17] Y.Y. Tong, C.D. Gu, J.L. Zhang, H. Tang, Y. Li, X.L. Wang, J.P. Tu, Urchin-like Ni-Co-P-O nanocomposite as novel methanol electro-oxidation materials in alkaline environment, Electrochim. Acta 187 (2016) 11–19, https://doi.org/10.1016/j.electacta.2015.10.195.

[18] X. Cui, P. Xiao, J. Wang, M. Zhou, W. Guo, Y. Yang, Y. He, Z. Wang, Y. Yang, Y. Zhang, Z. Lin, Highly branched metal alloy networks with superior activities for the methanol oxidation reaction, Angew. Chem. Int. Ed. 56 (2017) 4488–4493, https://doi.org/10.1002/anie.201701149.

[19] N.A.M. Barakat, M. Motlak, Co_xNi_y-decorated graphene as novel, stable and super effective non-precious electro-catalyst for methanol oxidation, Appl. Catal. B-Environ. 154–155 (2014) 221–231, https://doi.org/10.1016/j.apcatb.2014.02.019.

[20] R.J. Gorte, S. Park, J.M. Vohs, C. Wang, Anodes for direct oxidation of dry hydrocarbons in a solid-oxide fuel cell, Adv. Mater. 12 (2000) 1465–1469, https://doi.org/10.1002/1521-4095(200010)12:19<1465::AID-ADMA1465>3.0.CO;2-9.

[21] W.D. Hsu, M. Ichihashi, T. Kondow, S.B. Sinnott, Ab initio molecular dynamics study of methanol adsorption on copper clusters, J. Phys. Chem. A 111 (2007) 441–449, https://doi.org/10.1021/jp065669s.

[22] D. Zhao, R. Szostak, L. Kevan, Electron spin resonance and electron spin echo modulation spectroscopic studies of cupric ion − adsorbate interactions in synthetic clinoptilolite, J. Phys. Chem. B 101 (1997) 5382–5390, https://doi.org/10.1021/jp970700z.

[23] C.W. Lee, X. Chen, L. Kevan, Electron spin resonance and electron spin echo modulation studies of cupric ion location and adsorbate interactions in the copper (2+)-exchanged H-SAPO-11 molecular sieve, J. Phys. Chem. 95 (1991) 8626–8632, https://doi.org/10.1021/j100175a039.

[24] T.Z. Hong, Q. Xue, Z.Y. Yang, Y.P. Dong, Great-enhanced performance of Pt nanoparticles by the unique carbon quantum dot/reduced graphene oxide hybrid supports towards methanol electrochemical oxidation, J. Power Sources 303 (2016) 109–117, https://doi.org/10.1016/j.jpowsour.2015.10.092.

[25] Y. Sun, Y. Zhou, C. Zhu, L. Hu, M. Han, A. Wang, H. Huang, Y. Liu, Z. Kang, A Pt-Co_3O_4-CD electrocatalyst with enhanced electrocatalytic performance and resistance to CO poisoning achieved by carbon dots and Co_3O_4 for direct methanol fuel cells, Nanoscale 9 (2017) 5467–5474, https://doi.org/10.1039/C7NR01727H.

[26] Y. Liang, Y. Li, H. Wang, J. Zhou, J. Wang, T. Regier, H. Dai, Co_3O_4 nanocrystals on graphene as a synergistic catalyst for oxygen reduction reaction, Nat. Mater. 10 (2011) 780–786, https://doi.org/10.1038/nmat3087.

[27] K. Feng, J. Zhong, B. Zhao, H. Zhang, L. Xu, X. Sun, S.T. Lee, $Cu_xCo_{1-x}O$ nanoparticles on graphene oxide as a synergistic catalyst for high-efficiency hydrolysis of ammonia-Borane, Angew. Chem. Int. Ed. 55 (2016) 11950–11954, https://doi.org/10.1002/anie.201604021.

[28] H. Ming, Z. Ma, Y. Liu, K. Pan, H. Yu, F. Wang, Z. Kang, Large scale electrochemical synthesis of high quality carbon nanodots and their photocatalytic property, Dalton Trans. 41 (2012) 9526–9531, https://doi.org/10.1039/c2dt30985h.

[29] G. Jacobs, J.A. Chaney, P.M. Patterson, T.K. Das, J.C. Maillot, B.H. Davis, Fischer-Tropsch synthesis: study of the promotion of Pt on the reduction property of Co/Al_2O_3 catalysts by *in situ* EXAFS of Co *K* and Pt L_{III} edges and XPS, J. Synchrotron Radiat. 11 (2004) 414–422, https://doi.org/10.1107/S090904950401578X.

[30] H. Tian, X.L. Zhang, J. Scott, C. Ng, R. Amal, TiO2-supported copper nanoparticles prepared via ion exchange for photocatalytic hydrogen production, J. Mater. Chem. A 2 (2014) 6432–6438, https://doi.org/10.1039/C3TA15254E.

[31] I.G. Casella, Electrodeposition of cobalt oxide films from carbonate solutions containing Co(II)-tartrate complexes, J. Electroanal. Chem. 520 (2002) 119–125, https://doi.org/10.1016/S0022-0728(02)00642-3.

[32] I.G. Casella, M.R. Guascito, Electrochemical preparation of a composite gold–cobalt electrode and its electrocatalytic activity in alkaline medium, Electrochim. Acta 45 (1999) 1113–1120, https://doi.org/10.1016/S0013-4686(99)00315-1.

[33] W.K. Behl, J.E. Toni, Anodic oxidation of cobalt in potassium hydroxide electrolyte, J. Electroanal. Chem. 31 (1971) 63–75, https://doi.org/10.1016/S0022-0728(71)80043-8.

[34] L.D. Burke, M.E. Lyons, O.J. Murphy, Formation of hydrous oxide films on cobalt under potential cycling conditions, J. Electroanal. Chem. 132 (1982) 247–261, https://doi.org/10.1016/0022-0728(82)85022-5.

[35] Z. Zhang, Z. Luo, B. Chen, C. Wei, J. Zhao, J. Chen, X. Zhang, Z. Lai, Z. Fan, C. Tan, M. Zhao, Q. Lu, B. Li, Y. Zong, C. Yan, G. Wang, Z.J. Xu, H. Zhang, One-pot synthesis of highly anisotropic five-fold-twinned PtCu nanoframes used as a bifunctional electrocatalyst for oxygen reduction and methanol oxidation, Adv. Mater. 28 (2016) 8712–8717, https://doi.org/10.1002/adma.201603075.

[36] A. Maksic, Z. Rakocevic, M. Smiljanic, M. Nenadovic, S. Strbac, Methanol oxidation on Pd/Pt(poly) in alkaline solution, J. Power Sources 273 (2015) 724–734, https://doi.org/10.1016/j.jpowsour.2014.09.138.

[37] C. Shang, W. Hong, J. Wang, E. Wang, Carbon supported trimetallic nickel-palladium-gold hollow nanoparticles with superior catalytic activity for methanol electrooxidation, J. Power Sources 285 (2015) 12–15, https://doi.org/10.1016/j.jpowsour.2015.03.092.

[38] A. Serrà, E. Gómez, I.V. Golosovsky, J. Nogués, E. Vallés, Effective ionic-liquid microemulsion based electrodeposition of mesoporous Co–Pt films for methanol oxidation catalysis in alkaline media, J. Mater. Chem. A 4 (2016) 7805–7814, https://doi.org/10.1039/C6TA02035F.

[39] S. Zhang, H. Wang, N. Zhang, F. Kong, H. Liu, G. Yin, Role of Pt-pyridinic nitrogen sites in methanol oxidation on Pt/polypyrrole-carbon black Catalyst, J. Power Sources 197 (2012) 44–49, https://doi.org/10.1016/j.jpowsour.2011.09.031.